Experimental implementation of a multi-antenna 802.11ax-based passive bistatic radar for human target detection

Laurent Storrer*‡, Hasan Can Yildirim*, Evert Pocoma Copa*, Jérôme Louveaux†,
Philippe De Doncker*, Sofie Pollin‡, François Horlin*

*Université Libre de Bruxelles - †Université Catholique de Louvain - ‡Katholieke Universiteit Leuven
laurent.storrer@ulb.be, {Hasan.Can.Yildirim,Evert.Ismael.Pocoma.Copa}@vub.be, jerome.louveaux@uclouvain.be, sofie.pollin@kuleuven.be, {pdedonck,fhorlin}@ulb.ac.be

***Abstract*—We investigate and experimentally demonstrate a multi-antenna Wi-Fi-based passive bistatic radar (PBR) to perform indoor range-Doppler-angle detection of human targets. The latest Wi-Fi standard, 802.11ax, is considered as signal of opportunity, enabling a high range resolution suited for indoor detection. We build a Uniform-Linear-Array (ULA) using Universal Software Radio Peripherals (USRPs) as PBR receiver (RX), and present a novel calibration method to compensate the hardware-induced phase shift difference between the signals from the different antennas of the ULA. To avoid data association problems and limitations on the number of detectable targets for the Direction-of-Arrival (DoA) estimation, we demonstrate theoretically the possibility to use only the cell of the target in the radar range-Doppler maps (RDMs) across antennas as input to the Multiple Signal Classification (MUSIC) algorithm, rather than using the raw received signals. We validate the experimental setup and the processing by detecting the range, speed and DoA of two human targets moving in a room.**

***Index Terms*—Passive radar, Wi-Fi, 802.11ax, OFDM, SIMO, multi-antenna, MUSIC, Phase calibration**

I. Introduction

Remote monitoring with Wi-Fi signals has gained a lot of attention recently with the creation of the Task Group for Wi-Fi Sensing [1]. One of the main goals consists of indoor people movements monitoring and object detection, with various applications such as movement classification [2], intruder detection [3] or security staffs assistance in public buildings [4].

It is possible to perform indoor monitoring following a passive bistatic radar (PBR) approach. Radars can estimate the distance of targets based on multipath components (MPCs) propagation time (*range processing*) and the speed of targets thanks to the Doppler effect (*Doppler/speed processing*). In passive bistatic radar, the transmitter TX is a non-cooperative source of opportunity, not colocated with RX. One can thus create a Wi-Fi-based PBR by using a Wi-Fi access point (AP) as TX to reuse opportunistically existing signals for radar purposes. Wi-Fi signals are an interesting source of opportunity thanks to their quasi-ubiquitous availability and to their Orthogonal Frequency-Division Multiplexing (OFDM) modulation that is convenient for radar processing [3].

If the PBR features one single antenna at RX, it outputs a so-called *range-Doppler map* (RDM) or range-speed map, a 2D map where targets are identified by amplitude peaks. A radar chain to obtain the RDM using a 2D cross-correlation function is presented in [3]. However this work relies on old versions of 802.11 standards featuring a low bandwidth (< 20 MHz), yielding a range resolution above 10 m, which is not suited for indoor monitoring. Our recent works perform range and speed processing separately in a *decoupled approach* with channel estimation and Doppler Fast Fourier Transform (FFT) respectively and leverage the 802.11ac Wi-Fi standard, featuring a bandwidth up to 160 MHz, to obtain a range resolution of 0.9375 m [5], [6].

For indoor monitoring it is usually more convenient to detect a target in cartesian (*x*-*y*) coordinates to have the position of the target in a given environment. In that case, range and speed are not sufficient and the target angle, *i.e.* Direction-of-Arrival (DoA), needs to be computed. It can be computed by resorting to a multistatic PBR [7] or a multi-antenna PBR. We investigate this second option through the practical implementation of a multi-antenna Uniform Linear Array (ULA) PBR, *i.e.* featuring several antennas following an ULA pattern at RX. Based on the phase difference between the received signals at the different antennas, it allows to estimate the DoA with only one receiver by using the Multiple Signal Classification (MUSIC) algorithm [8].

There are three main challenges to deal with. Firstly, the different receiver hardware chains in a multi-antenna system induce random phase shifts between RX antennas, preventing the computation of the DoA. Secondly, in the presence of strong static MPCs, multiple targets or false alarms, performing MUSIC on the raw signals would yield a MUSIC angle spectrum featuring several peaks, one for each of these elements. It would require an extra step of data association between the peaks in the RDM and the peaks in the MUSIC spectrum. Furthermore, if RX features N_A antennas, the maximum number of DoAs that can be estimated is limited to $N_A - 1$ [9]. Thirdly, angle processing requires a strong target SNR to avoid the useful phase shift between antennas due to

DoA to be strongly affected by noise. However, human targets feature a small reflectivity which causes difficulty to achieve the required SNR. Our contribution is twofold:

- We demonstrate the usage of the latest Wi-Fi standard, 802.11ax [10], for human target detection with PBR applications by using the High-Efficiency Long-Training-Field (HE-LTF) present in the Preamble of each 802.11ax Wi-Fi packet. It allows the usage of a bandwidth of 80 MHz yielding a range resolution of 1.875 m, suited for indoor monitoring. For DoA estimation, we tackle the low target reflectivity problem by formalizing analytically how MUSIC can be applied per target at the output of the RDM to leverage the whole radar chain processing gain. This method also addresses the second challenge mentioned hereabove.
- We demonstrate experimentally the implementation of a multi-antenna ULA PBR allowing to perform range-Doppler-angle detection, enabling detection in Cartesian coordinates. We propose a novel *over-the-air* calibration method that can be performed during the radar processing itself for each measurement to compensate hardware-induced phase shifts between RX antennas by exploiting empty subcarriers imposed by the 802.11 standard around baseband DC in the OFDM spectrum [10].

This paper is structured as follows: in Section II and Section III, the system model and radar processing steps are summarized. In Section IV, the new calibration method and an experimental validation are presented. As a convention, lowercase letters correspond to the time-domain signals (*e.g.* x), and uppercase letters to the frequency-domain signals (*e.g.* X). Bold uppercase letters denote matrices or tensors of time-domain signals (*e.g.* $\mathbf{X}$), and bold uppercase calligraphic letters denote matrices or tensors corresponding to frequency-domain signals (*e.g.* $\boldsymbol{\mathcal{X}}$).

II. System model

It is considered that one Wi-Fi packet is transmitted continuously $N.M$ times (where M is an averaging factor detailed in III-A), in which the first OFDM symbol is a fully standard-compliant symbol from the HE-LTF of the Preamble of a 802.11ax Wi-Fi packet [10]. This replicates the behavior of a Wi-Fi access points transmitting packets in which only training OFDM symbols are known and usable for radar processing. The HE-LTF contains known complex PSK symbols, each placed on one of the Q OFDM subcarriers in the frequency domain. An Inverse Fast Fourier Transform (IFFT) is performed to obtain one time domain HE-LTF OFDM symbol [11]. The transmitted stream can be represented by a matrix $\mathbf{X}$ where each column, denoted with an index $k = 0, 1, ..., N.M-1$ (often called *slow time* index), is one OFDM symbol:

$$\mathbf{X}[i,k] = \frac{1}{\sqrt{Q}} \sum_{q=-Q/2}^{Q/2-1} \boldsymbol{\mathcal{X}}[q,k]\ e^{j2\pi qi/Q} \tag{1}$$

and

- $\boldsymbol{\mathcal{X}}$ is the matrix of frequency-domain PSK symbols;
- $q = -Q/2, ..., Q/2-1$ is the OFDM subcarrier index;
- $i = 0, 1, ..., Q-1$ is the time samples index (often called *fast time* index).

Before transmission, a Cyclic Prefix (CP) of length L is appended to each OFDM symbol [10]. The size of one time-domain OFDM symbol is thus $Q+L$. By defining the bandwidth of the system as B, the time between two consecutive samples is $T_s = 1/B$. The time between the reception of two HE-LTF symbols is defined as $T = (\kappa+1)(Q+L)T_s$, where κ is the number of unknown data OFDM symbols in the packet.

Each target r creates a multipath component (MPC) in the environment, starting from TX and arriving on each antenna $l = 0, 1, ..., N_A-1$ of RX, where N_A is the total number of RX antennas. Here only the first reflection MPC of the target is considered, characterized by the following elements:

- The complex amplitude α_r of the MPC. The path loss difference between the first antenna and the other antennas of the ULA is negligible.
- The DoA θ_r of the MPC.
- The propagation delay τ_r of the MPC from TX to the first antenna of the ULA. It corresponds to the bistatic distance $d_r = d_{TX-target} + d_{target-RX}$. The corresponding discrete time instant being the closest to the continuous delay value is $i_r \approx \left\lfloor \frac{\tau_r}{T_s} \right\rceil$. This is an approximation since the propagation time of the MPC between the first antenna and the others can be neglected for the distance computation. However it cannot be neglected in phase terms, *i.e.* complex exponentials. The bistatic distance can be estimated from i_r as $d_r = i_r T_s c$, with c being the speed of light in vacuum.
- The Doppler frequency shift $f_r = \frac{2v_r}{\lambda}\varepsilon_r$, with λ being the wavelength and $-1 \leq \varepsilon_r \leq 1$ an unknown projection factor depending on the bistatic geometry. The absolute value $|\varepsilon_r|$ is maximized when the target moves perpendicularly to the baseline TX-RX [12].

A channel impulse response (CIR), discretized into delay bins, models the environment containing mobile targets and stationary elements. Since RX holds multiple-antennas, there is one CIR per RX antenna l. The CIRs also change between the different received HE-LTF symbols due to Doppler shifts. Hence, there is one CIR per transmitted HE-LTF symbol, for each antenna at RX. The different CIRs containing this information can be stacked in a 3D tensor $\mathbf{H}$ whose elements are [11]:

$$\mathbf{H}[i,k,l] = \sum_{\tau_r \in \text{ bin } i} \alpha_r\ e^{-j2\pi f_c \tau_r}\ e^{j2\pi l\Delta sin(\theta_r) + j\Phi_l}\ e^{j2\pi f_r kT}, \tag{2}$$

with f_c the carrier frequency and $\Delta = \delta_{ant}/\lambda$ where δ_{ant} is the spacing between two antennas of the ULA. The exponential $e^{j2\pi l\Delta sin(\theta_r)}$ comes from the phase shift induced by the extra propagation delay of the MPC between the first antenna and the others, that depends on its DoA θ_r. Φ_l is the phase shift introduced by the receiver hardware chain connected to the l-th antenna: the phase-locked-loop, amplifiers and filters each introduce a phase shift [13]. The total resulting phase shift

cannot be predicted and is modelled as a random variable Φ_l that has to be calibrated, *i.e.* set as identical for all antennas l before angle processing, as described in section IV-B. A channel transfer function (CTF) tensor can also be defined as the FFT of the first dimension of $\mathbf{H}$, and denoted as the tensor $\boldsymbol{\mathcal{H}}$, with elements $\boldsymbol{\mathcal{H}}[q,k,l]$. Based on the CIR and CTF model, the values θ_r, d_r and v_r are thus to be estimated for each target r through the radar processing, explained in section III.

III. Radar Processing

A. Range Processing

Range processing is the estimation of d_r. Time-domain received symbols are the convolution of one CIR with the corresponding OFDM symbol. This is equivalent to a product in the frequency domain, yielding

$$\boldsymbol{\mathcal{Y}}[q,k,l] = \boldsymbol{\mathcal{H}}[q,k,l] \,.\, \boldsymbol{\mathcal{X}}[q,k] \;+\; \boldsymbol{\mathcal{W}}[q,k,l] \quad \forall q,k,l, \quad (3)$$

where $\boldsymbol{\mathcal{Y}}$ is the 3D tensor of the frequency-domain received signal for each antenna l for each transmitted OFDM symbol with index k. $\boldsymbol{\mathcal{W}}$ is a 3D tensor in which each vector $\boldsymbol{\mathcal{W}}[:,k,l] \quad \forall k,l$ of the first dimension is the FFT of a i.i.d. sequence of Additive White Gaussian Noise samples with a standard deviation ς. The operator $.$ denotes an element-wise product between all l-th frontal slabs $\boldsymbol{\mathcal{H}}[:,:,l]$ ($l = 0, 1, ..., N_A - 1$) of $\boldsymbol{\mathcal{H}}$ and the matrix $\boldsymbol{\mathcal{X}}$.

CIRs can be estimated with those received symbols. The frequency domain CTF for each OFDM symbol is estimated by Frequency-Domain Least-Squares Estimation [11]:

$$\hat{\boldsymbol{\mathcal{H}}}[q,k,l] = \boldsymbol{\mathcal{Y}}[q,k,l] \,/\, \boldsymbol{\mathcal{X}}[q,k] \quad \forall q,k,l, \quad (4)$$

where the operator $/$ denotes an element-wise division between all l-th frontal slabs $\boldsymbol{\mathcal{Y}}[:,:,l]$ ($l = 0, 1, ..., N_A - 1$) of $\boldsymbol{\mathcal{Y}}$ and the matrix $\boldsymbol{\mathcal{X}}$. Then, if the Doppler shift is sufficiently small so that a constant phase can be assumed over M packets, which is the case for walking human targets, the CTFs are averaged by groups of M to reduce the impact of noise [12]. The estimated time-domain CIRs are finally obtained by an IFFT on the first dimension of $\hat{\boldsymbol{\mathcal{H}}}$, *i.e.* one IFFT per averaged OFDM symbol, yielding the *radar cube* (RC):

$$\hat{\mathbf{H}}[i,k',l] = \frac{1}{\sqrt{Q}} \sum_{q=-Q/2}^{Q/2-1} \left(\frac{1}{M} \sum_{k=(k'-1)M}^{k'M-1} \hat{\boldsymbol{\mathcal{H}}}[q,k,l] \right) e^{j2\pi qi/Q} \quad (5)$$

$$= \mathbf{H}[i,k',l] + \widetilde{\boldsymbol{W}}[i,k',l] \quad (6)$$

where $k' = 0, 1, ..., N-1$ is the averaged OFDM symbol index corresponding to discrete time MT. The last exponential term from (2) becomes thus $e^{j2\pi f_r k' MT} \quad \forall k'$ in (6). The term

$$\widetilde{\boldsymbol{W}}[i,k',l] = \frac{1}{\sqrt{Q}} \sum_{q=-Q/2}^{Q/2-1} \left(\frac{1}{M} \sum_{k=(k'-1)M}^{k'M-1} \frac{\boldsymbol{\mathcal{W}}[q,k,l]}{\boldsymbol{\mathcal{X}}[q,k]} \right) e^{j2\pi qi/Q} \quad (7)$$

$\forall q,k,l$ is the remaining noise in the channel estimation. The RC contains the estimated delay $\hat{\tau}_r$ of each target r, yielding the target bistatic distance $\hat{d}_r = c\,\hat{\tau}_r$. If the distance between TX and RX is inferior to the range resolution $d_{res} = \frac{1}{2} c\, T_s$, then $\hat{d}_{target-RX} \approx \hat{d}_r/2$ by the quasi-monostatic assumption [14]. This is the case in this paper.

B. Speed processing

Speed processing is the estimation of v_r [12]. A N-point FFT is computed across the channel estimations, *i.e.* along the second dimension of the RC $\hat{\mathbf{H}}$. The time between two averaged channel estimations being MT, the frequency resolution of the FFT is $f_{res} = 1/(NMT)$. A Blackman window is applied prior to the FFT to reduce frequency leakage. This Doppler FFT yields one RDM per antenna, forming a range-Doppler-angle cube (RDAC), denoted $\hat{\mathbf{H}}_D$, whose elements are $\hat{\mathbf{H}}_D[i,n,l]$, where $n = 0, 1, ..., N-1$ is the frequency bin index of this FFT. In the RDAC, the Doppler frequency shifts $\hat{f}_r = \lfloor f_r / f_{res} \rceil \, f_{res}$ of the target are revealed for each tap. The speed can then be estimated with $\hat{v}_r = \hat{f}_r \lambda/2$. There is thus an error on the estimated speed due to the unknown projection factor ε_r. Elements for which $\hat{v}_r = 0$ are here referred to as static clutter and cancelled with *Average Removal* [6].

C. Angle processing

Angle processing is the estimation of θ_r. It relies on the phase shift $2\pi l \Delta sin(\theta_r)$ from (2) between the RX antennas. However the hardware-induced phase shift Φ_l is corrupting this antenna phase shift, requiring to perform a phase calibration prior to angle processing. This process is described in section IV-B, and it sets the phases Φ_l at the value of Φ_0 for all antennas, *i.e.* it takes the first antenna as reference to compensate the random phase variations. Angle processing is performed separately for each target r with MUSIC [8]. Given a detected target cell r at range tap i_r and frequency bin n_r, a $N_A \times 1$ vector $\mathbf{h}_r$ denoted as RDAC target vector is built:

$$\mathbf{h}_r = [\hat{\mathbf{H}}_D[i_r, n_r, 0] \; ... \; \hat{\mathbf{H}}_D[i_r, n_r, N_A - 1]]^T \quad (8)$$

It contains the RDAC cell of the target across antennas $l = 0, ..., N_A - 1$. This vector is used as input to MUSIC. Firstly, we prove that the RDAC target vector contains sufficient information to be able to compute the target DoA, *i.e.* that the phase difference between antennas is still present at this stage. By neglecting the noise term in the RC $\hat{\mathbf{H}}$ from (6) and considering that the phase Φ_l has been calibrated to Φ_0 for each antenna l, the Doppler FFT applied on $\hat{\mathbf{H}}$ gives the RDAC expressed as follows:

$$\hat{\mathbf{H}}_D[i,n,l] = \frac{1}{\sqrt{N}} \sum_{k'=-N/2}^{N/2-1} \hat{\mathbf{H}}[i,k',l] e^{-j2\pi k' n/N} \quad (9)$$

$$= \frac{1}{\sqrt{N}} \sum_{\tau_r \in \text{ bin } i} \alpha_r \; e^{-j2\pi f_c \tau_r} \; e^{j2\pi l \Delta sin(\theta_r) + j\Phi_0} \cdot \sum_{k'=-N/2}^{N/2-1} e^{j2\pi f_r k' MT} e^{-j2\pi k' n/N}. \quad (10)$$

The last term of (10) is the N-point FFT of the exponential $e^{j2\pi f_r k' MT} = e^{j2\pi (f_r/f_{res}) \cdot (k'/N)}$. If $f_r/f_{res} = n_r \in \mathbb{Z}$, *i.e.* if

the target Doppler frequency is exactly on a FFT bin, this term yields a Kronecker delta $\delta[n - n_r]$. If $f_r/f_{res} \notin \mathbb{Z}$ the term becomes $\text{sinc}(\pi(n - f_r/f_{res}))$ and there is frequency leakage. For the sake of simplicity of the final expression the first case is considered here. By taking the RDAC points of indices i_r and n_r to build $\mathbf{h}_r$, the term becomes $\delta[n_r - n_r] = 1$. The final expression of the RDAC points used to build $\mathbf{h}_r$ is thus

$$\hat{\mathbf{H}}_D[i_r, n_r, l] = \frac{1}{\sqrt{N}} \sum_{\tau_{r'} \in \text{ bin } i_r} \alpha_r \, e^{-j2\pi f_c \tau_{r'}} \, e^{j2\pi l \Delta sin(\theta_{r'}) + j\Phi_0} \tag{11}$$

Multiple targets having close values of range and speed could be detected as one unique RDAC cell r. That is, one RDAC target vector r could contain multiple targets, denoted as r' in (11) to differentiate them. Thus, the targets r' in the RDAC cell r have the same range $\hat{d}_{r'} = \hat{d}_r$ and the same speed $\hat{v}_{r'} = \hat{v}_r$ but different DoAs $\theta_{r'}$. In (11), the term $e^{j2\pi l \Delta sin(\theta'_r)}$ containing the phase difference between antennas is still present in the cell containing the target(s). Hence, it is possible to use the RDAC target vector to compute the DoA(s).

Vector (8) is used as input to MUSIC: an estimate of the target signal covariance matrix is computed as $\hat{\mathbf{R}}_r = \mathbf{h}_r \mathbf{h}_r^T$. The eigenvalues decomposition of $\hat{\mathbf{R}}_r$ is computed. Eigenvectors are divided into two submatrices, U_s and U_n, whose span are the signal and noise subspaces, respectively [8]. The corresponding N_A eigenvalues λ_j ($j = 0, 1, ..., N_A - 1$) are also separated in signal and noise eigenvalues:

$$\hat{\mathbf{R}}_r = \mathbf{U}\mathbf{\Lambda}\mathbf{U}^H_{|r} = [\mathbf{U}_s \mathbf{U}_n] \left[\begin{array}{c|c} \Lambda_s + \sigma^2 I_{K_r} & 0 \\ \hline 0 & \sigma^2 I_{N_A - K_r} \end{array} \right] \begin{bmatrix} \mathbf{U}_s^H \\ \mathbf{U}_n^H \end{bmatrix}_{|r} \tag{12}$$

where I is the identity matrix and $\sigma = (1/M)\,\varsigma$ is the variance of the noise in the RDAC $\hat{\mathbf{H}}_D$, with the $1/M$ factor being the noise variance reduction between the received signal and the RDAC due to averaging. K_r is the number of signal sources (here the targets) in vector $\mathbf{h}_r$. It can be superior to 1 if one cell detected as one target by the radar contains in reality several targets r', as said above. The diagonal matrix Λ_s contains the K_r eigenvalues associated to the signal sources. The other eigenvalues are noise eigenvalues.

The value of K_r is computed by using Eigenvalue Thresholding (ET) [9]. ET is an hypothesis test performed on the eigenvalues of $\hat{\mathbf{R}}_r$ ordered in descending order: a noise threshold is computed for each eigenvalue, and the MUSIC order K_r is set as the index of the first eigenvalue being superior to its corresponding threshold [9].

Then, the MUSIC DoA pseudo-spectrum

$$J^{-1}_{MUSIC}(\theta) = \frac{1}{\mathbf{a}(\theta)^H \mathbf{U}_n \mathbf{U}_n^H \mathbf{a}(\theta)} \tag{13}$$

is computed with $\mathbf{a}(\theta) = [1 \; e^{j2\pi\Delta sin(\theta)} \; ... \; e^{j2\pi(N_A-1)\Delta sin(\theta)}]^T$ the *array response vector*. The K_r local maxima of the DoA pseudo-spectrum are the estimated DoAs $\theta_{r'}$ of the targets r'. This process is repeated for each detection in the RDAC.

D. Other possible angle processing methods

Although it could seem unusual to estimate the covariance matrix $\hat{\mathbf{R}}_r$ with only one sample (the RDAC target vector), this estimated $\hat{\mathbf{R}}_r$ is close to the true $\mathbf{R}_r$. This is due to the high target-SNR, *i.e.* the ratio between the target peak power and the noise power floor in the RDAC, because of the radar processing gain. Indeed, the M-point averaging divides the noise power by M without affecting the target power. The N-point Doppler FFT, scaled by a factor $1/\sqrt{N}$ as in (11), multiplies the target power by N and doesn't affect the noise power. The target-SNR is thus multiplied by a factor NM. The presence of a high target-SNR is demonstrated in section IV-C. There are also two other possibilities of different inputs to give to MUSIC, each discarded for reasons explained herebelow:

- **RDAC row [12]:** It is possible to provide a $N_A \times N$ matrix consisting of the i_r-th horizontal slab $\hat{\mathbf{H}}_D[i_r, :, :]$ of the RDAC, *i.e.* the target horizontal RDAC slab, as input to MUSIC. This approach is discarded for two reasons. Firstly, the target FFT frequency leakage affects the MUSIC spectrum. Secondly, if there are multiple targets at the same range bin, *i.e.* the same row in the RDAC, there will be several peaks in the MUSIC spectrum which have to be correctly associated each with the correct peak in the RDAC.
- **RC row [12]:** It is also possible to provide a $N_A \times N$ matrix consisting of the i_r-th horizontal slab $\hat{\mathbf{H}}[i_r, :, :]$ of the RC, *i.e.* the target horizontal RC slab, as input to MUSIC. This approach is also discarded for two reasons. Firstly, it does not take advantage of the processing gain N provided by the Doppler FFT. The second reason is identical to the one of the RDAC row approach.

On the contrary, our approach benefits from the FFT gain, allowing to detect low reflectivity targets like humans. It also avoids the impact of the leakage and isolates the targets from each other. It doesn't require peak association since the peaks of each MUSIC spectrum all correspond to one RDAC cell. Once the range, speed and angle processing is complete, one could use this information to locate the target in Cartesian coordinates with $\hat{x}_r = \frac{\hat{d}_r}{2} \cos(\hat{\theta}_r)$ and $\hat{y}_r = \frac{\hat{d}_r}{2} \sin(\hat{\theta}_r)$.

IV. Experimental results

A. Setup

The experimental setup features one TX antenna and $N_A = 4$ RX antennas. It uses four USRPs X310: one for the TX antenna, two for the four RX antennas, and one as calibration anchor, described in section IV-B. The USRPs are all connected to one computer with 10 Gigabit Ethernet cables. Useful signal parameters for the experiment are given in I.

TABLE I
Experimental parameters

f_c	B	N	M	κ	Q	L	T
2.3 GHz	80 MHz	128	12	10	1024	256	176 μs

To demonstrate the viability of this work for multiple targets detection, there are two human targets moving in the environment. At the measurement instant, Target 1 is located at

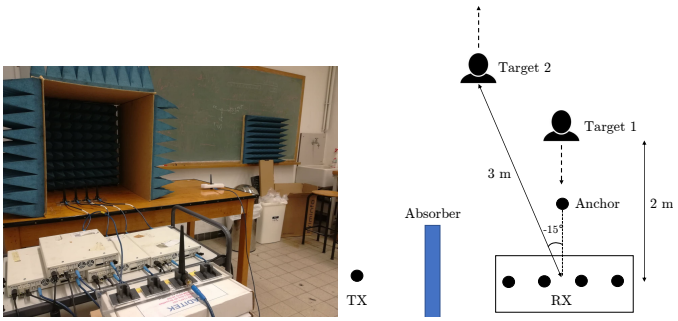

Fig. 1. Experimental setup

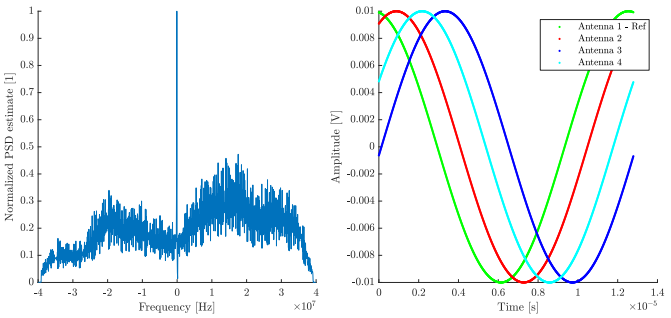

Fig. 2. Estimated baseband PSD of the received signal at the first antenna (left). Imaginary part of the CEs in time domain (right).

2 meters from RX with an angle of 0° and is moving towards RX at a speed of 1 m/s. Its detected speed should thus be positive. Target 2 is located at 3 meters from RX with an angle of -15° and is moving away from RX at a speed of 1 m/s. Its detected speed should thus be negative. The ground truth distances are measured with a lasermeter, and the ground truth speeds are obtained by computing the travelled distance by the target over one second around the measurement instant and assuming constant speed during this second. The measurement environment and the targets are illustrated on Figure 1.

B. Calibration

The hardware-induced phase shift Φ_l from (2) is preventing the angle processing to work. Calibration is the process of setting this phase at the common value of Φ_0 for all antennas, *i.e.* take the first antenna as reference and cancel the phase differences $\Phi_0 - \Phi_l, \quad l = 1, ..., N_A - 1$. By doing this, the only phase difference remaining between antennas is $2\pi l \Delta sin(\theta_r)$, which is the only relevant phase difference for angle processing. Here calibration takes place directly on the received signal before any processing.

Our new calibration method exploits the fact that in 802.11 standards, the OFDM subcarriers around baseband DC are left empty: in 802.11ax, the subcarriers $q \in [-2, 2]$ do not contain any PSK symbol [10]. A complex exponential at the frequency f_{cal} of one of these empty subcarriers, *i.e.* at OFDM subcarrier index $q_{cal} = f_{cal}\ Q/B \in [-2, 2]$, can be transmitted from a different device than TX. This device is here called *anchor*, and the exponential is denoted as *CE (calibration exponential)*. TX, RX and the anchor share the same clock to avoid CFO. The anchor is placed in front of the RX array, as illustrated on Fig. 1, so that its DoA θ w.r.t. to the array is identical and equal to 0° at each RX antenna in the far field. At RX, the received signal spectrum is a superposition of the OFDM spectrum, coming from MPCs of targets each with a DoA θ_r, and a peak at the subcarrier frequency corresponding to the CE frequency coming with a DoA equal to 0°. This principle is similar to what is presented in [13]. The peak of the CE is clearly noticeable in the estimated Power Spectral Density (PSD) of the received signal on the left of Figure 2.

Each antenna l receives a CE. Since it is present at one known unique subcarrier of index q_{cal}, the exponential spectrum can be extracted from each antenna without requiring any filtering, by saving the coefficient of that subcarrier, *i.e.* by building a $Q \times N_A$ matrix

$$\mathbf{S}[q, l] = \begin{cases} 0 & \text{if } q \neq q_{cal} \\ \boldsymbol{\mathcal{Y}}[q_{cal}, 1, l] & \text{if } q = q_{cal} \end{cases} \tag{14}$$

with the first OFDM symbol $k = 1$. Then by taking an IFFT on each column of $\mathbf{S}$ the time domain exponential of each antenna is obtained. CEs are not affected by the phase shift due to DoA since their DoA is 0°, they are only affected by the phase shift Φ_l. This is illustrated by plotting the imaginary part of the measured CEs on the right of Figure 2. The phase shift difference $\Phi_0 - \Phi_l$ creates a sample offset Δ_l between the CEs of antennas $l = 1, ..., N_A - 1$ and the first antenna $l = 0$, with the following relation:

$$\Phi_0 - \Phi_l = 2\pi f_{cal} \Delta_l T_s. \tag{15}$$

Δ_l can be computed by substracting the sample index of the maximum of the l-th exponential and the one of the first exponential. The corresponding difference $\Phi_0 - \Phi_l$ can then be deduced by (15). By multiplying the received signal tensor $\boldsymbol{\mathcal{Y}}[q, k, l]$ with the scalar $\exp(2\pi f_{cal} \Delta_l T_s)\ \forall l$, the hardware-induced phase shift difference $\Phi_0 - \Phi_l$ is thus cancelled. After this procedure, the CEs are removed from $\boldsymbol{\mathcal{Y}}[q, k, l]$ and the rest of the processing takes place.

C. Detection results

A zoom of the RDM of the first antenna is displayed on the left side of Figure 3. The two targets are highlighted with black rectangles. It can be noticed that high intensity spurious responses are present around each target. They are due to two elements. Firstly the residual Doppler FFT leakage, present on the frequency bins neighboring the target bin. Secondly the sidelobes along range dimension due to the frequency guard, *i.e.* the empty subcarriers in the OFDM spectrum. This sidelobes problem is addressed in [5].

To discriminate targets from noise in the RDM, one could use Constant False-Alarm Rate (CFAR) thresholding. However CFAR would produce several false-alarms due to the spurious returns mentioned above. This is why the targets are detected

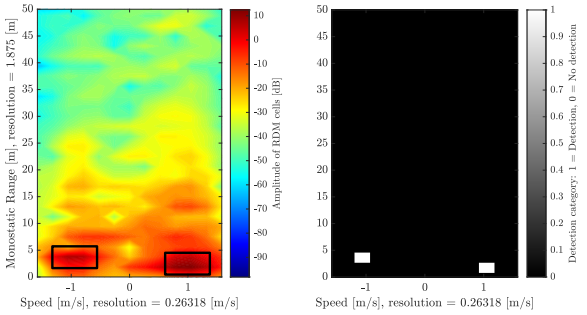

Fig. 3. RDM (left) and detection map (right) from the first antenna

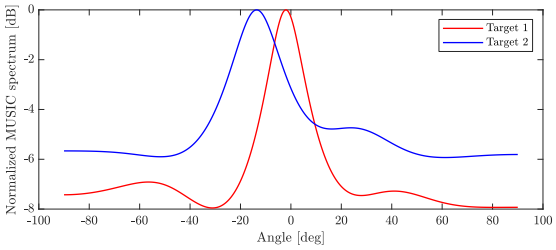

Fig. 4. MUSIC angle spectrum of the two targets

by performing a local maxima search on the RDM, yielding a detection map displayed on the right of Figure 3. It can be seen that following this approach the two targets are detected and separated from their surrounding spurious returns.

Finally, to determine the angle, one instance of MUSIC is applied on each detected target. As discussed in section III-C, the target-SNR is very high, allowing to estimate the covariance matrix $\hat{\mathbf{R}}_r$ with precision with the RDAC target vector as unique sample. Indeed, the target-SNR processing gain in dB is here $10\log_{10}(NM) = 31.86$ dB. From the first antenna RDM, the target-SNR for Target 1 and Target 2 is computed as 77.91 dB and 71.98 dB respectively.

The MUSIC order K_r is computed with ET. For the first target, the covariance matrix eigenvalues are $129.26, 1.47e^{-14}, 5.55e^{-15}$ and $2.01e^{-15}$. Intuitively, it is noticed that the 3 last eigenvalues are extremely small and thus correspond to noise. This is confirmed by ET that yields a MUSIC order $K_1 = 1$. ET also gives $K_2 = 1$ for the second target with covariance matrix eigenvalues $39.36, 7.94e^{-15}, 9.64e^{-16}$ and $1.30e^{-16}$. There are thus $K_1 + K_2 = 2$ detected targets, corresponding to the real number of targets. The resulting MUSIC spectra are plotted on Figure 4. The maximal value of each spectrum corresponds to the DoA of the target.

By combining Figures 3 and 4, the detected quasi-monostatic range, speed and DoA for Target 1 and Target 2 are summarized in II. It can be seen that they correspond to the real target values, with small errors being caused by the finite resolution of the radar processing steps. In particular, the two targets have the same measured speed in absolute value, while they have different angles and thus different projections $|\varepsilon_r|$ in absolute value. This is due to the fact that $|\varepsilon_1|$ and $|\varepsilon_2|$ are

TABLE II
TARGETS RANGE, SPEED AND DOA

	$\hat{d}_r/2$	$\hat{v}_r$	$\hat{\theta}_r$
Resolution	1.875 m	0.263 m/s	/
Target 1	1.875 m	1.053 m/s	-2.0°
Target 2	3.75 m	-1.053 m/s	-13.6°

close to each other since the two targets move perpendicularly to the baseline with a small difference in DoA. The difference $|\hat{v}_1| - |\hat{v}_2|$ is thus inferior to the speed resolution.

V. CONCLUSION

In conclusion, we demonstrated the feasibility of building a multi-antenna ULA Wi-Fi-based PBR with USRPs to perform indoor range-Doppler-angle detection of human targets using 802.11ax Wi-Fi signals. We proposed new solutions to deal with hardware non-idealities and multiple targets DoA estimation and validated them on a real-life scenario featuring multiple human targets.

REFERENCES

[1] IEEE 802.11, "Wi-Fi sensing," 2019, Last consultation: February 2020. [Online]. Available: https://mentor.ieee.org/802.11/documents?is_dcn=DCN%2C%20Title%2C%20Author%20or%20Affiliation&is_group=SENS

[2] B. Tan, K. Woodbridge, and K. Chetty, "A wireless passive radar system for real-time through-wall movement detection," *IEEE Transactions on Aerospace and Electronic Systems*, vol. 52, no. 5, pp. 2596–2603, October 2016.

[3] P. Falcone, F. Colone, and P. Lombardo, "Potentialities and challenges of wifi-based passive radar," *IEEE Aerospace and Electronic Systems Magazine*, vol. 27, no. 11, pp. 15–26, November 2012.

[4] C. Wang, J. Liu, Y. Chen, H. Liu, and Y. Wang, "Towards in-baggage suspicious object detection using commodity wifi," *2018 IEEE Conference on Communications and Network Security (CNS)*, pp. 1–9, 2018.

[5] H. C. Yildirim, L. Storrer, M. V. Eechkhaute, C. Desset, J. Louveaux, and F. Horlin, "Passive radar based on 802.11ac signals for indoor object detection," in *2019 16th European Radar Conference (EuRAD)*, 2019, pp. 153–156.

[6] L. Storrer, H. C. Yildirim, C. Desset, M. Bauduin, A. Bourdoux, and F. Horlin, "Clutter removal for WiFi-based passive bistatic radar," in *Accepted for presentation at IEEE VTC Spring 2020*, 2020.

[7] P. Falcone, F. Colone, A. Macera, and P. Lombardo, "Localization and tracking of moving targets with wifi-based passive radar," in *2012 IEEE Radar Conference*, May 2012, pp. 0705–0709.

[8] R. Schmidt, "Multiple emitter location and signal parameter estimation," *IEEE Transactions on Antennas and Propagation*, vol. 34, no. 3, pp. 276–280, March 1986.

[9] W. Chen, K. M. Wong, and J. P. Reilly, "Detection of the number of signals: a predicted eigen-threshold approach," *IEEE Transactions on Signal Processing*, vol. 39, no. 5, pp. 1088–1098, May 1991.

[10] Aruba Networks, "White paper: 802.11ax," 2019, Last consultation: February 2020. [Online]. Available: https://www.arubanetworks.com/assets/wp/WP_802.11AX.pdf

[11] Y. S. Cho, J. Kim, W. Y. Yang, and C. G. Kang, *MIMO-OFDM Wireless Communications with MATLAB*. Wiley Publishing, 2010.

[12] M. Richards, W. Holm, and J. Scheer, *Principles of Modern Radar: Basic Principles*, ser. Electromagnetics and Radar. Institution of Engineering and Technology, 2010. [Online]. Available: https://books.google.be/books?id=nD7tGAAACAAJ

[13] S. Monfared, T.-H. Nguyen, T. Van der Vorst, P. De Doncker, and F. Horlin, "Experimental Demonstration of AoA Estimation Uncertainty for IoT Sensor Networks," in *Accepted for presentation at IEEE VTC Spring 2020*, 2020.

[14] D. Jenn, "Radar Fundamentals," 2008, naval Postgraduate School, Department of Electrical and Computer Engineering.